Crystal-Momentum-Resolved Contributions to Harmonics in Laser-Driven Graphene

Zhaoyang Peng(彭朝阳)[1], Yue Lang(郎跃)[1], Yalei Zhu(朱雅蕾)[1], Jing Zhao(赵晶)[1], Dongwen Zhang(张栋文)[1], Zengxiu Zhao(赵增秀)[1*], and Jianmin Yuan(袁建民)[1,2*]

[1]*Department of Physics, National University of Defense Technology, Changsha 410073, China*
[2]*Department of Physics, Graduate School of China Academy of Engineering Physics, Beijing 100193, China*

(Received 13 March 2023; accepted manuscript online 6 April 2023)

We investigate the crystal-momentum-resolved contributions to high-order harmonic generation in laser-driven graphene by semi-conductor Bloch equations in the velocity gauge. It is shown that each harmonic is generated by electrons with the specific initial crystal momentum. The higher harmonics are primarily contributed by the electrons of larger initial crystal momentum because they possess larger instantaneous energies during the intraband motion. Particularly, we observe circular interference fringes in the crystal-momentum-resolved harmonics spectrum, which result from the inter-cycle interference of harmonic generation. These circular fringes will disappear if the inter-cycle interference is disrupted by the strong dephasing effect. Our findings can help to better analyze the mechanism of high harmonics in graphene.

DOI: 10.1088/0256-307X/40/5/054203

High harmonic generation (HHG) is an important nonlinear optical effect that occurs when a material is subjected to a high-intensity laser field, which results in the production of attosecond photonics and coherent extreme ultraviolet sources.[1,2] Beyond the fruitful research in atomic gases, HHG is studied extensively in solid-phase targets in the past decade,[3–6] including crystals, amorphous solids,[7,8] and two-dimensional materials.[9–11] Due to the rich information encoded in HHG, it is of potential applications to investigate the ultrafast electron dynamics in solids[12,13] and to probe the electronic structure, such as the band structure,[14,15] Berry curvature,[16,17] and topology.[18,19]

In early studies, solid-phase HHG was simulated by the response of a single valence electron (such as electron at the Γ point).[20,21] However, it has been reported that HHG is intrinsically contributed by all the electrons in the first Brillouin zone at sufficiently high laser intensities.[22] Therefore, it is worth examining the individual contribution of each electron and the interference between them. Some studies have investigated the crystal-momentum-resolved contributions to harmonics and found that different plateaus of HHG are generated by electrons with varying initial crystal momenta.[23] In addition, pairs of electrons with opposite crystal momenta can result in destructive interference of even-order harmonics in crystals with inversion symmetry.[24] Moreover, the formation of recollision quantum orbits depends critically on the interference between harmonics produced by different crystal momentum channels.[25]

Graphene is a two-dimensional material consisting of carbon atoms arranged in a honeycomb lattice, with a unique electronic band structure known as the Dirac cone.[26] The linear dispersion relation near the Dirac point results in a fixed group velocity for electrons, which is only dependent on the direction of the crystal momentum. Due to the zero energy gap, even weak fields can produce a strongly nonlinear optical response. Experimental observations have reported harmonics up to the ninth order and demonstrated an unique ellipticity dependence of HHG.[9] In this Letter, we use the semi-conductor Bloch equations (SBEs) in the velocity gauge to study the crystal-momentum-resolved contributions to harmonics. In the velocity gauge, the dynamics of electrons with different initial crystal momentums are independent under the dipole approximation, which allows us to resolve their individual contributions to each harmonic. The results show that the crystal momentum dependence of harmonics varies under different driving ellipticities and each harmonic is dominated by electrons with specific initial momentum. Meanwhile, further analysis on the dynamical phase of electrons reveals that the inter-cycle interference causes circular fringes in the crystal-momentum-resolved spectrum, which will disappear under strong dephasing effect.

Theoretical Model. We use the SBEs in velocity gauge to calculate the radiation from graphene driven by strong laser fields according to Refs. [9,10,27]. The unique electronic band structure of graphene is characterized by the gapless Dirac cones at the Dirac points in the Brillouin zone. When the laser intensity is not too high, only electrons near the Dirac points are significantly excited, and their ultrafast dynamics can be accurately described by the massless Dirac Hamiltonian. The two-component Dirac Hamiltonian in the laser field $\boldsymbol{A}(t)$ is given by

$$\hat{H}_{\rm e} = \hbar v_{\rm F} \hat{\boldsymbol{\sigma}} \cdot [\boldsymbol{k} + e\boldsymbol{A}(t)], \tag{1}$$

where $v_{\rm F}$ is the Fermi velocity of the electron, $\hat{\boldsymbol{\sigma}} = (\hat{\sigma}_x, \hat{\sigma}_y)$ is the Pauli operator, and $\boldsymbol{k} = (k_x, k_y)$ is the crystal momentum. When the laser pulse is absent, the Hamiltonian exhibits eigen-energies $\varepsilon_{\pm} = \pm\hbar v_{\rm F}\sqrt{k_x^2 + k_y^2}$, which represent the energy levels of two distinct bands formed at

*Corresponding authors. Email: zhaozengxiu@nudt.edu.cn; jmyuan@gscaep.ac.cn
© 2023 Chinese Physical Society and IOP Publishing Ltd

the Dirac points. This corresponds to the gapless Dirac cone with a linear dispersion relation. The electrons' group velocity is therefore fixed and only dependent on the direction of the crystal momentum. The eigenvectors of the Hamiltonian are $\varphi_{\mathrm{v},\boldsymbol{k}} = (1/\sqrt{2})[-1, \exp(\theta_{\boldsymbol{k}})]^{\mathrm{T}}$ and $\varphi_{\mathrm{c},\boldsymbol{k}} = (1/\sqrt{2})[1, \exp(\theta_{\boldsymbol{k}})]^{\mathrm{T}}$, where $\theta_{\boldsymbol{k}} = \arctan(k_y/k_x)$ is the polar angle of the wavevector $\boldsymbol{k}$. These eigenvectors correspond to the Bloch basis of the valence and conduction bands, which are denoted by v and c, respectively.

The SBE in the velocity gauge is given by [9,10]

$$\dot{\boldsymbol{\rho}}_{\boldsymbol{k}} = -\frac{i}{\hbar}[\boldsymbol{H}_{\boldsymbol{k}}, \boldsymbol{\rho}_{\boldsymbol{k}}] + \boldsymbol{L}(\boldsymbol{\rho}_{\boldsymbol{k}}), \tag{2}$$

where the density matrix $\boldsymbol{\rho}_{\boldsymbol{k}}$ is defined as $(\boldsymbol{\rho}_{\boldsymbol{k}})_{ij}(t) = \langle \Omega(t)|\hat{b}^{\dagger}_{j,\boldsymbol{k}}\hat{b}_{i,\boldsymbol{k}}|\Omega(t)\rangle$. The $\hat{b}_{\mathrm{v},\boldsymbol{k}}$ and $\hat{b}_{\mathrm{c},\boldsymbol{k}}$ are annihilation operators for electrons in the valence band and conduction band, respectively. The $|\Omega(t)\rangle$ indicates the time-dependent state of electrons in laser pulse. We suppose that the electrons are initially in the ground state, in which the valence band is fully occupied and the conduction band is completely empty. This is described by the initial density matrix with $(\boldsymbol{\rho}_{\boldsymbol{k}})_{\mathrm{vv}}(t_0) = 1$ and all other matrix elements being zero. The matrix $\boldsymbol{H}_{\boldsymbol{k}}$ is given by $(\boldsymbol{H}_{\boldsymbol{k}})_{ij} = \langle \varphi_{i,\boldsymbol{k}}|\hat{H}_{\mathrm{e}}|\varphi_{j,\boldsymbol{k}}\rangle$. The second term in Eq. (2) is introduced to account for the decoherence effect, which is defined as $(\boldsymbol{L})_{\mathrm{vc}} = -(\boldsymbol{\rho}_{\boldsymbol{k}})_{\mathrm{vc}}/T_2$, $(\boldsymbol{L})_{\mathrm{cv}} = -(\boldsymbol{\rho}_{\boldsymbol{k}})_{\mathrm{cv}}/T_2$ and $(\boldsymbol{L})_{\mathrm{vv}} = -(\boldsymbol{L})_{\mathrm{cc}} = (\boldsymbol{\rho}_{\boldsymbol{k}})_{\mathrm{cc}}/T_1$ in our calculation, where T_1 and T_2 are depopulation and dephasing times, respectively. In graphene, the dephasing and depopulation times are regarded as a few tens of femtoseconds and a few picoseconds, respectively. [9,10,28]

The average current from the electron with initial crystal-momentum $\boldsymbol{k}$ is given by $\boldsymbol{j}_{\boldsymbol{k}} = (e/m)\mathrm{Tr}[\boldsymbol{\rho}_{\boldsymbol{k}}\boldsymbol{\sigma}]$, where the matrix $\boldsymbol{\sigma}$ is defined as $(\boldsymbol{\sigma})_{ij} = \langle \varphi_{i,\boldsymbol{k}}|\hat{\boldsymbol{\sigma}}|\varphi_{j,\boldsymbol{k}}\rangle$. Specifically, the matrix $\boldsymbol{\sigma}$ is given by

$$\sigma_x = \begin{pmatrix} -\cos\theta_{\boldsymbol{k}} & -i\sin\theta_{\boldsymbol{k}} \\ i\sin\theta_{\boldsymbol{k}} & \cos\theta_{\boldsymbol{k}} \end{pmatrix}, \ \sigma_y = \begin{pmatrix} -\sin\theta_{\boldsymbol{k}} & i\cos\theta_{\boldsymbol{k}} \\ -i\cos\theta_{\boldsymbol{k}} & \sin\theta_{\boldsymbol{k}} \end{pmatrix}. \tag{3}$$

The total current is obtained by summing the individual currents for each crystal momentum, i.e., $\boldsymbol{j}(t) = \sum_{\boldsymbol{k}} \boldsymbol{j}_{\boldsymbol{k}}(t)$. The spectrum thus can be obtained by the Fourier spectrum of the time-dependent current

$$I(\omega) \sim \omega^2|\boldsymbol{j}(\omega)|^2 = \omega^2\Big|\sum_{\boldsymbol{k}} \boldsymbol{j}_{\boldsymbol{k}}(\omega)\Big|^2. \tag{4}$$

In our calculation, the laser pulse is modeled as

$$\begin{aligned} \boldsymbol{A}(t) &= [A_x, A_y] \\ &= A_0 f(t)\frac{1}{\sqrt{1+\epsilon^2}}[\cos(\omega_0 t), \epsilon\sin(\omega_0 t)], \end{aligned} \tag{5}$$

where ϵ is the ellipticity of laser pulse, $A_0 = E_0/\omega_0$ represents the peak strength of the laser pulse, and $f(t)$ is the sin-square temporal envelope with the duration of 10 cycles. We use a mid-infrared laser pulse with a photon energy of 0.26 eV and a peak field strength of $E_0 = 0.0002$ a.u. The atomic units are used in the following text. The relaxation constants are set to $T_1 = 16T$ and $T_2 = 1.6T$ with T being the laser period, as specified in Refs. [9,10].

Numerical Result. Figures 1(a) and 1(b) present the intensities of harmonics for pump ellipticities of $\epsilon = 0$ and $\epsilon = 0.3$, respectively. We can observe odd harmonic peaks up to the ninth order, with intensities decreasing as the harmonic order increases. When the laser pulse is linearly polarized ($\epsilon = 0$), the harmonic polarization is aligned with the laser polarization. In contrast, for an elliptically polarized laser pulse, the harmonics can be observed in both the x and y directions. Figures 1(c) and 1(d) show the ellipticity dependence of the 5th and 7th harmonics intensities, respectively, with normalization to the linearly polarized intensity ($\epsilon = 0$). It can be seen that the harmonic intensities in the y direction are enhanced in the elliptically polarized pulse, reaching a maximum around $\epsilon = 0.3$. These results suggest that HHG in graphene is enhanced at a finite laser ellipticity, which differs significantly from gas-phase HHG, where the highest production is observed in a linearly polarized pumping. These features of HHG in graphene have been observed in the experiment, [9] which indicates the validity of our approach.

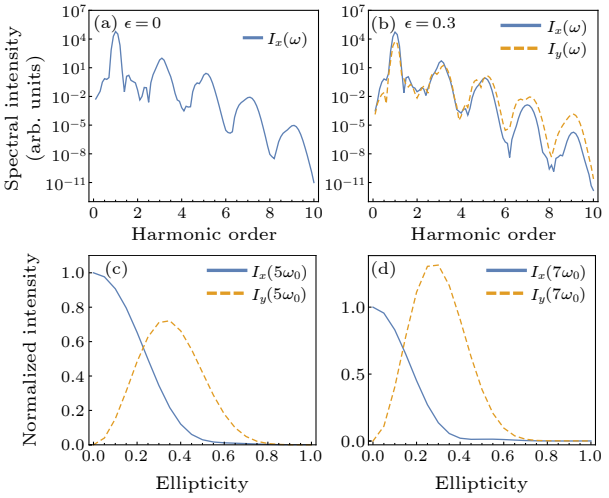

Fig. 1. The spectrum in x and y directions for pump ellipticities of (a) $\epsilon = 0$ and (b) $\epsilon = 0.3$; and the dependence of the intensity of (c) 5th and (d) 7th on the driven ellipticity.

Figure 2 illustrates the crystal-momentum-resolved spectrum for the 3rd, 5th and 7th harmonics, i.e., $\omega^2|\boldsymbol{j}_{\boldsymbol{k}}(n\omega_0)|^2$. The three harmonics show a distinct crystal momentum dependence. A closer look at the crystal-momentum-resolved spectrum in Fig. 2 reveals a series of circular fringes with discontinuities. These circular fringes represent regions in k space where the electron is most likely to participate in the HHG process. As can be seen, the range of circular fringes expands with harmonic order, which suggests that higher order harmonics are generated from electrons with larger initial $\boldsymbol{k}_0$ values. In addition, the circular fringes in the elliptically polarized pumping are more complete compared to those in the linearly polarized pumping, which enables more electrons in k space to contribute to the generation of harmonics. This effect becomes more pronounced as the ellipticity of the laser pulse increases, which affects the dependence of high-harmonic generation in graphene on the ellipticity of the pumping field. [29–32]

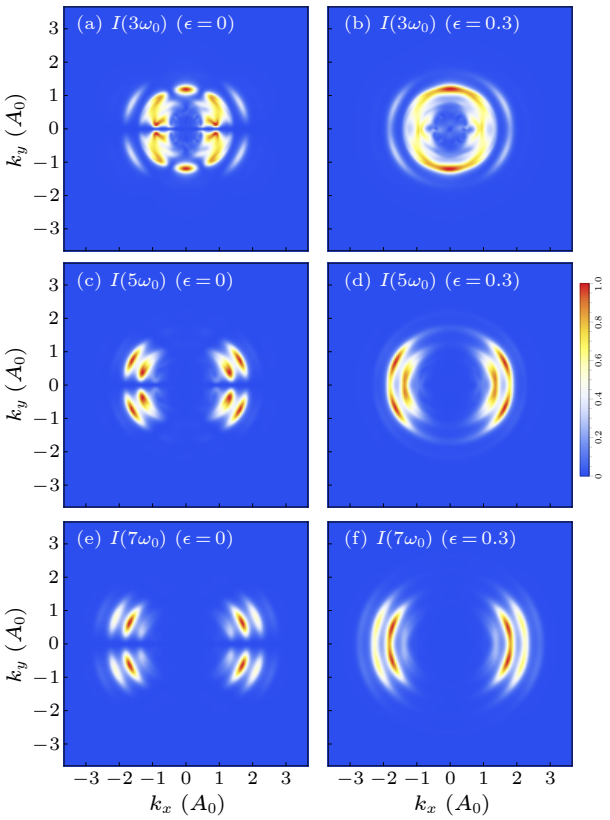

Fig. 2. Normalized crystal-momentum-resolved contribution to the 3rd, 5th, and 7th harmonics with driving ellipticities of $\epsilon = 0$ and $\epsilon = 0.3$.

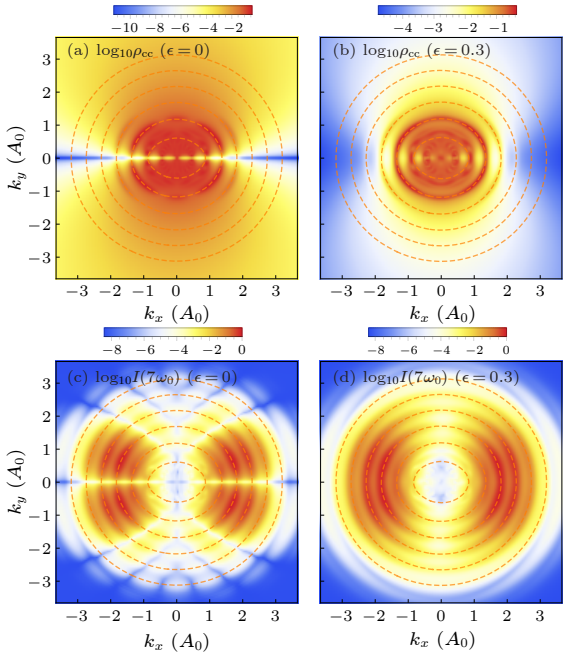

Fig. 3. [(a), (b)] The final occupation of the conduction band in the logarithm plot. [(c), (d)] The normalized crystal-momentum-resolved spectrum of the 7th harmonic in the logarithm plot. Dashed lines show the theoretical momentum allowing constructive inter-cycle interference with $\phi(\boldsymbol{k}_0) = 2n\pi$, which agrees well with the circular fringes observed in simulations.

Figures 3(a) and 3(b) depict the final occupation of the conduction band at the end of the laser pulse, revealing a series of similar circular fringes. However, it is not always the case that the region in k space with the stronger excitation contributes more significantly to HHG. For instance, the circular fringe that contributes the most to the 7th harmonic has a larger radius than those exhibiting the strongest excitation, as shown in Figs. 3(c) and 3(d).

To analyze the crystal-momentum-resolved contribution to each harmonic, we employ the classical three-step model in k space, which is commonly used to describe HHG in solid-phase targets.[21,33–38] First, the electron with initial crystal momentum $\boldsymbol{k}_0$ moves in the k space according to the acceleration theorem, i.e., $\boldsymbol{k}(t) = \boldsymbol{k}_0 + \boldsymbol{A}(t)$. Figure 4(a) shows an example of intra-band movement in the case of linearly polarized pumping, where the red point indicates the location of the initial momentum and the yellow line indicates the range of intra-band movement. When the instantaneous energy is at its lowest, the electron can be excited into the conduction band, after which it will continuously move within that band. Figure 4(b) shows the corresponding instantaneous energy of the electron during the intra-band movement. When the instantaneous energy gap equals the energy of harmonic photons, the electron can recombine in the valence band and emit harmonics in the corresponding order. Therefore, the electrons with larger initial $\boldsymbol{k}_0$ values can acquire higher instantaneous energy and emit higher order harmonics, although electrons with smaller initial $\boldsymbol{k}_0$ values are more likely to be excited into the conduction band due to smaller energy gaps.

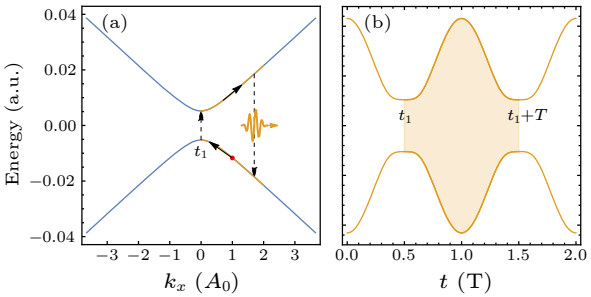

Fig. 4. (a) Sketch of the the classical three-step model of the HHG in graphene. The blue line show the k_x-dependent band structure with the fixed $k_y = 0.5A_0$. The red point indicates the electron's initial momentum ($k_x = A_0$, $k_y = 0.5A_0$). The solid arrows indicate the intra-band motion, while the dashed arrows indicate inter-band transition. (b) The instantaneous energy of the electron as it moves in the valence and conduction band. The shaded area corresponds to the dynamic phase accumulated during one optical cycle as given by Eq. (7).

In addition to instantaneous energy, the inter-cycle interference also affects crystal-momentum-resolved contribution to harmonics. Since electrons are driven by multi-cycle laser pulses, the excitation can occur in each laser cycle and the probability amplitude from each cycle must be coherently summed, leading to the inter-cycle interference. The interference pattern can be visualized more clearly using a logarithmic plot, as illustrated in Fig. 3. Assuming that the time-profile of the laser pulse can be neglected, the probability of electron excitation in each cycle is equivalent. Thus, the inter-cycle interference is determined by

the phase difference between the probability amplitudes of two adjacent excitation paths, which is given by [39–41]

$$\Phi(\boldsymbol{k}_0) = \frac{\pi}{2} - \frac{\pi}{2}\mathrm{sign}\Big(\frac{E(t_1+T)}{E(t_1)}\Big) + \phi(\boldsymbol{k}_0), \tag{6}$$

where $E(t_1)$ and $E(t_1+T)$ indicate the electric field at the two time instants of excitation. The first two terms correspond to the transition and propagation phases, while the third term represents the dynamical phase accumulated during the intra-band motion, as shown by the shaded area in Fig. 4(b). In the case of inter-cycle interference, the sum of the first two terms is zero. Therefore, the phase difference is solely determined by the dynamical phase, which is given by

$$\phi(\boldsymbol{k}_0) = \int_{t_1}^{t_1+T} \varepsilon_+(t) - \varepsilon_-(t)\, d\tau, \tag{7}$$

where $\varepsilon_\pm(t) = \pm v_\mathrm{F}|\boldsymbol{k}(t)|$ represent the instantaneous energies of electron as it moves in the valence band and conduction band along the trajectory $\boldsymbol{k}(t) = \boldsymbol{k}_0 + \boldsymbol{A}(t)$. We have assumed that the temporal envelope $f(t)$ in $\boldsymbol{A}(t)$ can be neglected, therefore the integral does not depend on t_1. If the dynamical phase accumulated between two adjacent cycles is an integer multiple of 2π, the excitation in each cycle can constructively interfere. Conversely, if the phase difference is an odd multiple of π, destructive interference occurs. Therefore, the position of the circular fringes can be determined based on the condition of constructive interference, i.e., $\phi(\boldsymbol{k}_0) = 2n\pi$, which are plotted with the dashed line in Fig. 3. As we can see, the dashed lines agree well with the location of circular fringes in the interference pattern, both for the 7th harmonic and for the final occupation of the conduction band. This confirms the validity of the picture of inter-cycle interference.

Note that the inter-cycle interference of excitation in the time domain can also be understood as the multiphoton excitation in the energy domain. [42] The results presented here suggest that electron excitation in such laser intensities is primarily dominated by the multiphoton process. Also, note that the excitation mechanism depends on both the laser intensity and excitation energy. In graphene, the excitation energy is k-dependent, resulting in a k-dependent excitation mechanism. As shown in Fig. 2(a), the circular fringes near the Dirac point deviate from a circle, indicating a transition in the excitation mechanism from the multiphoton regime to the tunneling regime.

Additionally, apart from the inter-cycle interference, the multiple excitation events within a laser cycle can lead to the intra-cycle interference. [40] The pattern of intra-cycle interference is characterized by the parabolic-like fringes that lead to discontinuities in the circular fringes, [42,43] as shown in Figs. 3(a) and 3(c) in the case of linearly polarized pumping. In contrast, in the case of elliptically polarized pumping, the electron's intra-band movement in the k space will follow a two-dimensional trajectory due to the ellipticity of the laser pulse. Therefore, the intra-cycle interference cannot occur for elliptically polarized pumping, as shown in Figs. 3(b) and 3(d).

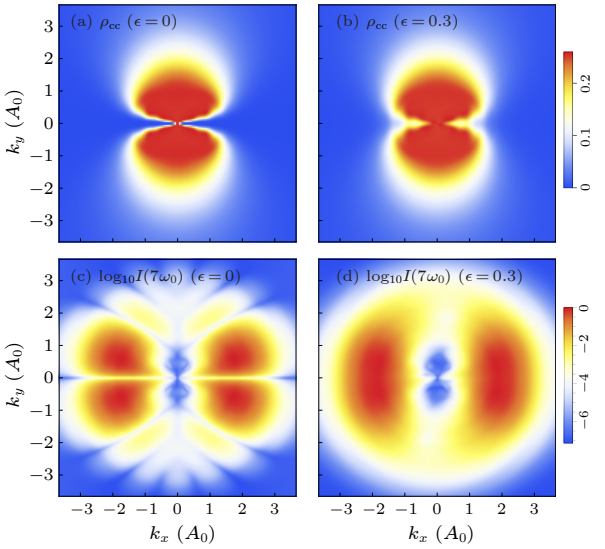

Fig. 5. [(a), (b)] The final occupation of the conduction band. [(c), (d)] The crystal-momentum-resolved spectrum of the 7th harmonic with a dephasing time of $T_2 = 0.3T$.

Finally, we discuss the influence of the dephasing effect, which is characterized by the dephasing time T_2. Dephasing is caused by electron–electron collisions or other decoherence effects, which lead to loss of coherence in electron dynamics. In the above simulation, the dephasing time is 1.6 laser pulse cycles, which ensures stable inter-cycle interference. However, if the dephasing effect is very strong, the dynamical phase of the electron will be distorted by the dephasing effect, leading to a breakdown of inter-cycle interference. Figure 5 display the crystal-momentum-resolved final occupation and spectrum of the 7th harmonic with a dephasing time of $T_2 = 0.3T$. It can be observed that the circular interference fringes arising from inter-cycle interference completely vanish for both the final occupation and 7th harmonic. Only the parabolic-like interference fringes resulting from the intra-cycle interference can be observed in the crystal-momentum-resolved spectrum of the 7th harmonic in the linearly polarized pumping. In addition, the crystal-momentum-resolved final population in the conduction exhibits similar patterns for two ellipticity values, as shown in Figs. 5(a) and 5(b). This is due to the fact that excitation process in such a short dephasing time is mainly determined by the sub-cycle dynamics of the electron. [44] Therefore, it is suggested that the dephasing time will severely affect the crystal momentum dependence of the harmonics by disrupting the inter-cycle interference.

In summary, we have investigated the crystal-momentum-resolved contributions to HHG in laser-driven graphene. Specifically, according to the three-step model in momentum space, the maximum instantaneous energy of an electron during the intra-band movement is determined by its initial crystal momentum. As a result, electrons with larger initial crystal momentums can emit higher order harmonics. Furthermore, the harmonic emission is also affected by the inter-cycle interference of multiple excitation events during the periodic intra-band movement. If the corresponding dynamical phase accumulated between the two excitation events in adjacent cycles is

an odd multiple of π, destructive interference will prohibit the harmonic emission. However, the inter-cycle interference can be disrupted by strong dephasing effect. Our study complements the understanding of HHG in graphene. These findings may be helpful for development of ultrafast optoelectronic devices based on graphene and other two-dimensional materials.

Acknowledgments. This work was supported by the National Key R&D Program of China (Grant No. 2019YFA0307703), the National Natural Science Foundation of China (Grant Nos. 12234020 and 12274384), and the Major Research Plan of the National Natural Science Foundation of China (Grant No. 91850201).

References

[1] Krausz F and Ivanov M 2009 *Rev. Mod. Phys.* **81** 163
[2] Wang X W, Wang L, Xiao F, Zhang D W, Lü Z H, Yuan J M, and Zhao Z X 2020 *Chin. Phys. Lett.* **37** 023201
[3] Ghimire S, DiChiara A D, Sistrunk E, Agostini P, DiMauro L F, and Reis D A 2011 *Nat. Phys.* **7** 138
[4] Ghimire S and Reis D A 2019 *Nat. Phys.* **15** 10
[5] Kruchinin S Y, Krausz F, and Yakovlev V S 2018 *Rev. Mod. Phys.* **90** 021002
[6] You Y S, Reis D A, and Ghimire S 2017 *Nat. Phys.* **13** 345
[7] Jürgens P, Liewehr B, Kruse B, Peltz C, Engel D, Husakou A, Witting T, Ivanov M, Vrakking M J J, Fennel T, and Mermillod-Blondin A 2020 *Nat. Phys.* **16** 1035
[8] You Y S, Yin Y, Wu Y, Chew A, Ren X, Zhuang F, Gholam-Mirzaei S, Chini M, Chang Z, and Ghimire S 2017 *Nat. Commun.* **8** 724
[9] Yoshikawa N, Tamaya T, and Tanaka K 2017 *Science* **356** 736
[10] Tamaya T, Ishikawa A, Ogawa T, and Tanaka K 2016 *Phys. Rev. Lett.* **116** 016601
[11] Tancogne-Dejean N and Rubio A 2018 *Sci. Adv.* **4** eaao5207
[12] Schubert O, Hohenleutner M, Langer F, Urbanek B, Lange C, Huttner U, Golde D, Meier T, Kira M, Koch S W, and Huber R 2014 *Nat. Photon.* **8** 119
[13] Ossiander M, Golyari K, Scharl K, Lehnert L, Siegrist F, Bürger J P, Zimin D, Gessner J A, Weidman M, Floss I, Smejkal V, Donsa S, Lemell C, Libisch F, Karpowicz N, Burgdörfer J, Krausz F, and Schultze M 2022 *Nat. Commun.* **13** 1620
[14] Lanin A A, Stepanov E A, Fedotov A B, and Zheltikov A M 2017 *Optica* **4** 516
[15] Li L, Lan P, He L, Cao W, Zhang Q, and Lu P 2020 *Phys. Rev. Lett.* **124** 157403
[16] Luu T T and Wörner H J 2018 *Nat. Commun.* **9** 916
[17] Banks H B, Wu Q, Valovcin D C, Mack S, Gossard A C, Pfeiffer L, Liu R B, and Sherwin M S 2017 *Phys. Rev. X* **7** 041042
[18] Reimann J, Schlauderer S, Schmid C P, Langer F, Baierl S, Kokh K A, Tereshchenko O E, Kimura A, Lange C, Güdde J, Höfer U, and Huber R 2018 *Nature* **562** 396
[19] Heide C, Kobayashi Y, Baykusheva D R, Jain D, Sobota J A, Hashimoto M, Kirchmann P S, Oh S, Heinz T F, Reis D A, and Ghimire S 2022 *Nat. Photon.* **16** 620
[20] Wu M X, Ghimire S, Reis D A, Schafer K J, and Gaarde M B 2015 *Phys. Rev. A* **91** 043839
[21] Wu M X, Browne D A, Schafer K J, and Gaarde M B 2016 *Phys. Rev. A* **94** 063403
[22] Navarrete F, Ciappina M F, and Thumm U 2019 *Phys. Rev. A* **100** 033405
[23] Yu C, Iravani H, and Madsen L B 2020 *Phys. Rev. A* **102** 033105
[24] Liu X, Li Y, Liu D, Zhu X, Zhang X, and Lu P 2021 *Phys. Rev. A* **103** 033104
[25] He Y L, Guo J, Gao F Y, Yang Z J, Zhang S Q, and Liu X S 2021 *Phys. Rev. A* **104** 013104
[26] Castro N A H, Guinea F, Peres N M R, Novoselov K S, and Geim A K 2009 *Rev. Mod. Phys.* **81** 109
[27] Guan Z, Liu L, Wang G L, Zhao S F, Jiao Z H, and Zhou X X 2020 *Chin. Phys. B* **29** 104206
[28] Heide C, Eckstein T, Boolakee T, Gerner C, Weber H B, Franco I, and Hommelhoff P 2021 *Nano Lett.* **21** 9403
[29] Tamaya T, Ishikawa A, Ogawa T, and Tanaka K 2016 *Phys. Rev. B* **94** 241107
[30] Liu C D, Zheng Y H, Zeng Z N, and Li R X 2018 *Phys. Rev. A* **97** 063412
[31] Feng Y, Shi S, Li J, Ren Y, Zhang X, Chen J, and Du H 2021 *Phys. Rev. A* **104** 043525
[32] Ren Y, Jia L, Zhang Y, Zhang Z, Xue S, Yue S, and Du H 2022 *Phys. Rev. A* **106** 033123
[33] Ikemachi T, Shinohara Y, Sato T, Yumoto J, Kuwata-Gonokami M, and Ishikawa K L 2017 *Phys. Rev. A* **95** 043416
[34] Li L, Lan P, Zhu X, Huang T, Zhang Q, Lein M, and Lu P 2019 *Phys. Rev. Lett.* **122** 193901
[35] Lang Y, Peng Z, Liu J, Zhao Z, and Ghimire S 2022 *Phys. Rev. Lett.* **129** 167402
[36] Lang Y, Peng Z, and Zhao Z 2022 *Chin. Phys. Lett.* **39** 114201
[37] Liu L, Zhao J, Dong W, Liu J, Huang Y, and Zhao Z 2017 *Phys. Rev. A* **96** 053403
[38] Liu L, Zhao J, Yuan J M, and Zhao Z X 2019 *Chin. Phys. B* **28** 114205
[39] Shevchenko S N, Ashhab S, and Nori F 2010 *Phys. Rep.* **492** 1
[40] Du T Y, Tang D, and Bian X B 2018 *Phys. Rev. A* **98** 063416
[41] Du T Y and Ding S J 2019 *Phys. Rev. A* **99** 033406
[42] Arbó D G, Ishikawa K L, Schiessl K, Persson E, and Burgdörfer J 2010 *Phys. Rev. A* **81** 021403
[43] Arbó D G, Ishikawa K L, Persson E, and Burgdörfer J 2012 *Nucl. Instrum. Methods Phys. Res. Sect. B* **279** 24
[44] Peng Q, Peng Z, Lang Y, Zhu Y, Zhang D, Lü Z, and Zhao Z 2022 *Chin. Phys. Lett.* **39** 053301